Electrochimica Acta 345 (2020) 136166

Contents lists available at ScienceDirect

Electrochimica Acta

journal homepage: www.elsevier.com/locate/electacta

ATR-FTIR in Kretschmann configuration integrated with electrochemical cell as in situ interfacial sensitive tool to study corrosion inhibitors for magnesium substrates

L.I. Fockaert [a, b], T. Würger [c, d], R. Unbehau [c], B. Boelen [e], R.H. Meißner [c, d], S.V. Lamaka [c], M.L. Zheludkevich [c], H. Terryn [f], J.M.C. Mol [b, *]

[a] Netherlands Organization for Scientific Research (NWO), Postbus 3021, 3502, GA, Utrecht, the Netherlands
[b] Delft University of Technology, Department of Materials Science and Engineering, Research Group Corrosion Technology and Electrochemistry, Mekelweg 2, 2628, CD, Delft, the Netherlands
[c] Magnesium Innovation Centre (MagIC), Helmholtz-Zentrum, Max-Planck-Straße 1, 21502, Geesthacht, Germany
[d] Hamburg University of Technology, Institute of Polymer and Composites, Denickestraße 15, 21073, Hamburg, Germany
[e] Tata Steel IJmuiden B.V., Research and Development, Surface Engineering – Coating Development, 1970, CA, IJmuiden, the Netherlands
[f] Vrije Universiteit Brussel, Department of Materials and Chemistry, Research Group Electrochemical Surface Engineering, Pleinlaan 2, 1050, Brussels, Belgium

ARTICLE INFO

Article history:
Received 4 November 2019
Received in revised form
25 March 2020
Accepted 31 March 2020
Available online 5 April 2020

Keywords:
Corrosion inhibitors
Magnesium
Integrated ATR-FTIR
EIS setup
Chemisorption
DFT

ABSTRACT

Integrated attenuated total reflection – Fourier transform infrared spectroscopy (ATR-FTIR) – Electrochemical impedance spectroscopy (EIS) measurements were used to simultaneously follow chemisorption mechanisms of organic inhibitors as well as their corrosion inhibition efficiency towards magnesium based substrates. Four carboxylic compounds, i.e. 2,5-pyridinedicarboxylic acid (PDC), 3-methylsalicylic acid (MSA), sodium salicylate (SS) and fumaric acid (FA), were selected based on their promising inhibiting capacities and were all shown to chemisorb at the $MgO/Mg(OH)_2$ surface by carboxylate bond formation. Orientation analysis using polarized infrared light showed that carboxylate bonds established using aliphatic carboxylate compound aligned perpendicular to the magnesium surface, whereas carboxylate bonds with aromatic compounds were oriented in plane with the magnesium surface. This different orientation is associated to the involvement of π-interactions in the $MgO/Mg(OH)_2$ – aromatic carboxylate adsorption. Additionally, DFT calculations revealed that the addition of hetero-atoms (i.e. N or OH) in the molecular structure contributes to increased adsorption energies, indicating that next to carboxylate groups also these hetero-atoms are involved in interfacial interactions. Integrating the ATR-FTIR setup with an electrochemical cell allowing for simultaneous EIS measurements lead to two surface phenomena determining the inhibition efficiency. Surface hydroxylation processes on one hand forming a $MgO/Mg(OH)_2$ layer on one hand, and the chemisorption of carboxylate compounds on the other hand. The inhibition efficiency was found to increase in following order: FA < PDC < MSA and was mainly associated to the formation of a $MgO/Mg(OH)_2$ layer. SS was shown to act as a corrosion accelerator rather than a corrosion inhibitor. Despite its high sensitivity for water, both surface processes could be followed in situ by means of ATR-FTIR. Simultaneously, protective properties of the formed films could be quantified by means of EIS. Consequently, integrated ATR-FTIR – EIS methodology has shown to be highly valuable for gaining in-situ insights in the inhibition mechanism, while quantifying the inhibition efficiency. This was even possible for highly active metal substrate as magnesium, although further developments are suggested if one aims to quantify electrochemical constants related to corrosion and other surface processes measured at the low frequencies (i.e. < 1 Hz).

1. Introduction

One of the most practical and economical ways to improve

* Corresponding author.
E-mail address: J.M.C.Mol@tudelft.nl (J.M.C. Mol).

https://doi.org/10.1016/j.electacta.2020.136166

corrosion resistance concerns the introduction of corrosion inhibitors. Typically, corrosion inhibitors are chemical compounds which promote the formation of an insoluble and stable layer at the surface [1]. However, due to its high activity, such effective compounds are limited for magnesium [2]. Magnesium is a lightweight material that is gaining more attention from industry. Its high abundancy together with its high-strength-to-weight ratio and ease of machining and recycling offers a wide range of applications [3,4]. Yet, its high intrinsic and microgalvanic corrosion susceptibility remains a major drawback limiting its implementation in industrial engineering. In order to find adequate corrosion inhibitors, fundamental insights on both inhibition efficiency and inhibiting mechanism are required. Quantification of the corrosion inhibition efficiency is generally obtained by means of electrochemical measurements, such as electrochemical impedance spectroscopy (EIS) and potentiodynamic polarization (PDP) measurements [5–10]. On the other hand, corrosion inhibition mechanisms are commonly derived using local techniques indicating the onset of corrosion and surface sensitive and/or vibrational techniques revealing the chemisorption mechanisms of protective species [11]. However, although electrochemical techniques demonstrate the time-dependency of corrosion inhibiting mechanisms, these studies are rarely accompanied with in situ chemical analysis [12–14]. This is primarily associated to the challenges that come with in situ measurements in aqueous media, which are not only faced using vacuum-techniques such as X-ray photoelectron spectroscopy or scanning electron microscopy, but also for scanning kelvin probe force measurements, where the interpretation of Volta potential values is complicated by the presence of water [15]. More recently, the use of in situ optical techniques has been reported to in situ monitor surface phenomena, such as the onset of corrosion [16]. Although the development of such approach was shown to provide valuable information for correct EIS data interpretation, it does not give molecular insights on the ongoing corrosion inhibiting mechanism. Consequently, up to now, there is still a need for a platform that offers in situ molecular insights on an interfacial level, without interference of bulk water and which is compatible with EIS measurements to simultaneously indicate the inhibition mechanisms and efficiency. Contrary to Fourier transform infrared spectroscopy (FTIR), in situ Raman is not sensitive for bulk water and has therefore been proposed as a promising vibrational tool to study chemisorption mechanisms in aqueous media without interference of prominent water signals [17]. Nonetheless, because of its low surface sensitivity its use is typically restricted to noble metals, as Ag, Au and Cu, which are known to create a surface enhancement effect resulting in extremely high surface sensitivity [18]. Promising efforts have been taken to extend the use of surface-enhanced Raman scattering (SERS) to other substrates [19–22]. Meanwhile, the capacities of in situ attenuated total reflection (ATR)-FTIR remained underexplored [15]. This is primarily associated to its high sensitivity for polar bonds giving dominant water signals that may interfere with the signal of interest [23]. Yet, due to its different selection rules, ATR-FTIR is highly complementary to Raman and can be used to study inhibition mechanisms involving both organic [7] and inorganic molecules [24,25]. However, next to its high sensitivity for bulk water, the requirement for IR-transparent and thus model metal substrates forms another limitation to the use of ATR-FTIR. Metals can be partially IR-transparent if they are being applied in thin nanolayers, for example by means of physical vapour deposition. However, exposure of such thin films to an aqueous environment is particularly challenging for active substrates such as magnesium. When this thin metal film is brought in direct contact with an internal reflection element (IRE) one speaks of ATR-FTIR in the Kretschmann configuration [26]. The IRE is characterized by a higher refractive index compared to the medium (e.g. air or electrolyte) above the metal, which results in total internal reflection of the incident IR-beam at the IRE-metal interface. During this internal reflection an evanescent wave is generated perpendicular to the IRE surface. The charges in the evanescent wave create an electric field that extends into medium above the metal surface, as shown in Fig. 1. The electric field polarizes the dielectric thereby inducing a second wave, referred to as the surface plasmon polariton [27]. This phenomenon reduces the intensity of reflected light explaining the name attenuated total reflection-FTIR. The accessibility of metal-electrolyte interfaces from the metal side allows for the integration of an electrochemical cell in the ATR-FTIR setup, creating the opportunity to monitor molecular phenomena at the surface, while simultaneously probing electrochemical properties such as oxide resistance and barrier properties [28–30]. Consequently, such an integrated setup could be very useful to gain fundamental in situ insights in inhibiting mechanism of corrosion inhibitors [7].

In addition to experimental work, density functional theory (DFT) calculations have shown to be useful for achieving a more comprehensive understanding of corrosion inhibition mechanisms and efficiencies [31–35]. DFT-computed parameters, such as the energy difference (ΔE_{HL}) between the highest occupied (HOMO) and the lowest unoccupied molecular orbital (LUMO), can describe the affinity of the corrosion inhibitors to transition metal ions, thus potentially indicating a relationship to the corrosion inhibition efficiency when the underlying inhibition mechanism is based on complex formation with corrosive species [10]. Further investigations of Seifzadeh et al. indicate ΔE_{HL} also to play a role in the complexation of Mg ions [36] as well as the adsorption on Mg-based alloys [37]. However, successful correlation of the HOMO-LUMO gap and inhibition efficiencies strongly depends on the investigated substrate, and hence a general relationship cannot be established [10,38–41]. Provided that the inhibitor adsorption is decisive for the inhibition efficiency, also adsorption energies derived from atomistic simulations can be an important parameter; strongly binding molecules would correlate with high inhibition efficiencies and vice versa [29]. Respective calculations are performed on model substrates, similar to ATR-FTIR. Yet, as simulations can be computationally rather demanding, the adsorption environment is often simplified by e.g. excluding the solvent, thus introducing discrepancies between theoretical and experimental conditions [42], which have to be taken into account. Hence, definition of the model requires sufficient attention in order to obtain

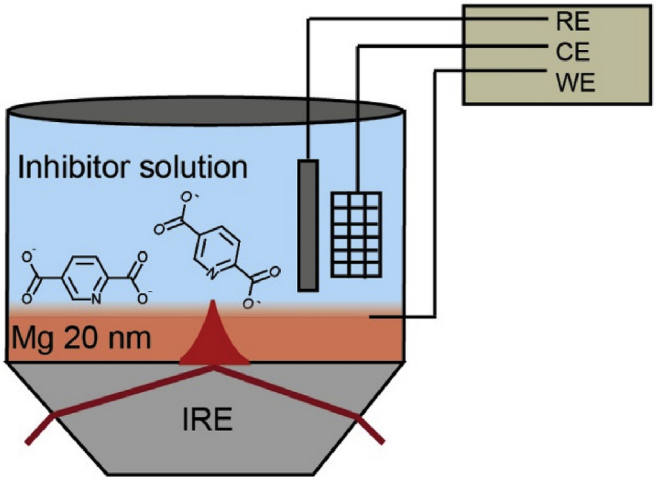

Fig. 1. Integrated ATR-FTIR – EIS approach for in situ studies on inhibition mechanism and efficiency of corrosion inhibitors for magnesium.

significant results [39].

A thorough systematic screening of 151 compounds, both inorganic and organic, was conducted on their corrosion inhibiting efficiency towards six magnesium alloys [8]. From this, 2,5-pyridinedicarboxylate, 3-methylsalicylate and fumarate, were suggested to be capable of forming complexes with iron cations and were subsequently more fundamentally studied, characterizing their corrosion product layers [2]. Two different trends in inhibiting mechanisms were observed, passivation of the surface by forming a protective film on one hand, and forming complexes with dissolved impurities, such as iron cations, on the other hand. The latter prevents redeposition of impurities more noble than magnesium which is a driving force for microgalvanic corrosion [43,44]. This lead to the insights that 3-methylsalicylate acts as a cathodic inhibitor, binding to iron cations impeding microgalvanic corrosion. Whereas 2,5-pyridinedicarboxylate and fumarate, despite their ability to form iron complexes, prominently showed anodic inhibiting behaviour by forming an adsorptive protective layer [2]. It is obvious that impurities and hence the susceptibility to microgalvanic corrosion play a crucial role in inhibition requirements for magnesium alloys.

This work aims to investigate the capabilities of the ATR-FTIR integrated with an electrochemical cell, allowing EIS measurements while monitoring vibrational oxide and adsorbate evolutions. In situ ATR-FTIR measurements were performed using s- and p-polarized IR-light to gain insights in the orientation of the inhibiting molecules when adsorbing to magnesium. In addition to molecular information for unravelling an adsorption mechanism, complementary EIS measurements were performed to measure oxide film resistances indicating the inhibiting performance. Moreover, DFT computations were performed for a more comprehensive understanding of the investigated inhibitor molecules at the magnesium surface. Here, the prevailing conditions in neutral to alkaline solutions, were mimicked by a proton exchange of the carboxylic acids at the MgO (100) surface, resulting in magnesium hydroxide and deprotonated carboxylates.

The ability of the integrated setup to simultaneously probe inhibition mechanisms and efficiency was validated on high purity (HP) magnesium in aqueous environments. Previously, the determining role of iron impurities on the corrosion mechanism of magnesium alloys has been extensively described. However, due to the application of thermally vaporized model substrates the contribution of iron impurities ($T_m = 1538\ ^\circ C$ at Patm) on thermally vaporized magnesium ($T_m = 650\ ^\circ C$ at Patm) substrates is expected to be negligible when using the integrated ATR-FTIR − EIS setup. Therefore, obtained inhibiting efficiencies are compared to previously reported results on magnesium alloys to validate the proposed approach for industrially relevant substrates used in the engineering applications.

2. Experimental

Materials and chemicals: Inhibitor solutions containing 0.05 M 2,5-pyridinedicarboxylic acid (>98%, Sigma-Aldrich Chemie GmbH),3-methylsalicylic acid (99%, Sigma-Aldrich Chemie GmbH), sodium salicylate (>99.5%, Sigma-Aldrich Chemie GmbH) and fumaric acid (98%, Alfa Aesar) were prepared in demineralized water. The pH of the inhibitor solutions was adjusted to pH 7 ± 0.3 using 1 M NaOH.

Magnesium films with a thickness of approximately 20 nm were thermally vaporized by means of physical vapour deposition (PVD) on germanium internal reflection elements (PIKE Technologies, 60°) by means of a high-vacuum evaporation system (VCM 600 Standard Vacuum Thermal Evaporator, Norm Electronics). The source material for the PVD substrates was resublimed pure Mg (a by-product during Mg sintering process), which composition is shown in Table 1. The high purity of the magnesium source used together with the low melting point of magnesium compared to the impurities present in the source material are expected to result in magnesium films with a level of impurities significantly lower than that in the source material.

Table 1
Elemental composition of high purity magnesium used in this work as a source of PVD.

Element	Al	Ca	Cu	Be	Fe	Mn	Ni	Si	Zn	Zr	Mg
Impurity level, ppm	<100	14	5	0.2	12	73	10	7	21	25	99,97%

Attenuated total reflection − Fourier transform infrared spectroscopy with integrated electrochemical cell for electrochemical impedance spectroscopy measurements: The FTIR apparatus was a Thermo-Nicolet Nexus equipped with a liquid-nitrogen cooled mercury-cadmium-telluride (MCT-A) detector and a nitrogen-purged measurement chamber with a Veemax III single reflection ATR accessory. IR-light was configured with an incident set angle of 80°. A precision manual polarizer (PIKE) was mounted on the Veemax III and set to 90° for p-polarized and 0° for s-polarized IR-light. Prior to the in situ chemisorption studies, infrared backgrounds were obtained of magnesium coated germanium internal reflection elements immersed in demineralized water. Subsequently, demineralized water was quickly replaced by the inhibitor-containing solution for in situ ATR-FTIR − EIS measurements. Infrared spectra were collected every 3 s and averaged from 16 cycles with a resolution of 4 cm^{-1}. The control of the spectra acquisition and data analysis (peak position and area quantification) was managed by the OMNIC 8.1 software package (Thermo-Electron Corporation, Madison, WI). EIS measurements were performed using a SI1286 electrochemical interface Solartron potentiostat over a frequency range from 10^5 to 10^{-1} Hz, 7 points per decade and a sinusoidal amplitude of 10 mV. This gives an analysis time of ca. 1.7 min per EIS cycle. On the other hand, ATR-FTIR data has been averaged from 16 spectra collected every 3 s, giving an intermediate time of 27 s. Time acquisition occurred upon immediate contact of magnesium substrate with solution. EIS measurements were conducted in the electrochemical cell of PIKE Technology designed for the Veemax III accessory, which has been in-house modified to reduce the exposed contact area to 1 cm^2, allowing the application of an electric connection outside the exposed contact area. As a result a conventional three-electrode setup was build, with a platina mesh as counter electrode and Ag/AgCl/sat. KCl (+0.197 V vs standard hydrogen electrode) as reference electrode. Impedance plots were recorded on at least three samples for each inhibitor solution and processed using Zview from Scribner Associates Inc.

Density functional theory computations: DFT computations were performed using the plane-wave code Vienna Ab Initio Simulation Package (VASP) [45] [−] [48] with the projector augmented wave (PAW) method. As van der Waals (vdW) interactions may have a significant impact on the adsorption energies of organic molecules [49], the exchange-correlation (XC) functional optB88-vdW [50−53] was employed for all DFT calculations in this study. This functional, which belongs to the group of van der Waals density functionals (vdW-DF), accounts for dispersion interactions by including a non-local correlation part in the exchange-correlation energy instead of using external input parameters. Still, some approximations are assumed, such as that the vdW interactions are considered to be pairwise additive. By optimizing the correlation part of the original vdW-DF by Langreth, Lundqvist and colleagues [54], Klimeš et al. introduced the “opt” functionals [50,51], which

have been successfully applied to numerous systems [55–62]. Particularly, the optB88-vdW functional is considered to represent well the subtle energetic contributions of weak interactions in the adsorption of organic molecules [63–65].

All computations were performed using a $4 \times 4 \times 1$ Γ-centered grid of *k*-points [66]. The plane-wave expansion was limited by a cutoff energy of 520 eV. During the relaxation process, the atomic positions were allowed to adjust until the Hellmann–Feynman forces were less than 5 meV $Å^{-1}$. For the relaxation process, the systems were pre-converged using the conjugate gradient algorithm; subsequently a quasi-Newton algorithm was employed, which is efficient close to a minimum. In a third computation step, the structure was investigated statically to obtain more accurate total energies via the tetrahedron method with Blöchl corrections [67].

The $MgO/Mg(OH)_2$ interface was modeled using a slab of five MgO(100) layers in a 2×2 surface cell. An illustration of the model along with some potential adsorption sites [68] on the Mg (100) surface can be found in the Supplementary Material. With respect to the number of carboxyl groups within the adsorbed inhibitor molecules, hydrogen atoms were co-adsorbed accordingly on the oxygen sites of the MgO(100) surface, resulting in a partially hydroxylated surface – representing the start of the passivation layer formation – and leaving the deprotonated inhibitor molecule to adsorb. Atoms in the two bottom layers were kept fixed in their bulk-like positions, whereas the remaining layers were free to relax, thus being able to respond to occurring forces due to adsorption or surface effects. A vacuum region of around 20 Å was added above the surface slab in order to avoid interaction between periodic images [69]. A dipole correction was applied to compensate for slab asymmetry [70,71]. The binding energies E_B of the adsorbed inhibitor molecules on the partially hydroxylated MgO(100) surface were determined as the difference between total energies of the educts, $E_{adsorbate,gas}$ and $E_{substrate}$, as well as the total energy of the product, $E_{subs+ads}$:

$$E_B = E_{adsorbate,gas} + E_{substrate} - E_{subs+ads}$$

Hence, for $E_B > 0$ the corresponding adsorption structure is energetically favorable and vice versa, assuming negative total energies.

3. Results

3.1. In situ ATR-FTIR kinetic study of magnesium in demineralized water without organic inhibitors

Fig. 1 presents the dynamic behaviour of magnesium in demineralized water without organic compounds. Broad bands at 3378 and 1670 cm^{-1}, specific to O–H stretching and bending modes illustrate the hydration of the surface during immersion in water. Furthermore, the higher wavenumber region is characterized by a sharp negative peak at 3700 cm^{-1} attributed to brucite, $Mg(OH)_2$ [72]. The sharpness of this characteristic peak relates to the absence of hydrogen bonds in this compound [3], whereas its negative intensity relative to the background (collected prior to immersion) relates to the conversion of brucite into species of which the hydroxide ions are involved in hydrogen bonds [3]. Meanwhile, additional vibrational bands appear at 1176 and 860 cm^{-1} consistent with the deformation of H_2O or OH^- [73]. Although all aqueous solutions are initially neutral, anodic dissolution reactions accompanied with cathodic oxygen reduction reactions generating hydroxide anions thereby locally increasing the pH to 10.5 [74]. Due to this instant local pH increase, rapid formation of $Mg(OH)_2$ is expected within seconds upon adding an aqueous electrolyte [74]. Formation of the $Mg(OH)_2$ is governed by the constant value of the solubility product. Local pH is buffered by formed $Mg(OH)_2$ as generated hydroxide ions (OH^-) are being consumed for the formation of $Mg(OH)_2$. In addition to the formation of a hydroxylation layer, two new peaks at 1382 and 1530 cm^{-1} arise upon prolonged immersion in demineralized water. The growth of these peaks is assigned to the formation of magnesium carbonate complexes originating from the presence of ambient CO_2 dissolved in the aqueous solution [72]. In Fig. 2 (b) the quantified peak areas of the Mg–OH peak at 1176 cm^{-1} and the summed peak area of the carbonate peaks positioned at 1530 and 1382 cm^{-1} are plotted as a function of immersion time. From these plots it is seen that native magnesium oxide rapidly hydroxylates upon immersion in demineralized water, reaching their maximum intensity after 1.2 min, where after they decline again. Meanwhile carbonate peaks assigned to magnesium carbonate complexes are being formed. However, their reducing peak intensities upon prolonged submersion illustrate that neither the magnesium hydroxide layer, nor the magnesium carbonate layer are stable in the aqueous environment. The poor stability of hydroxide layers formed during immersion of magnesium in neutral aqueous environment has been reported

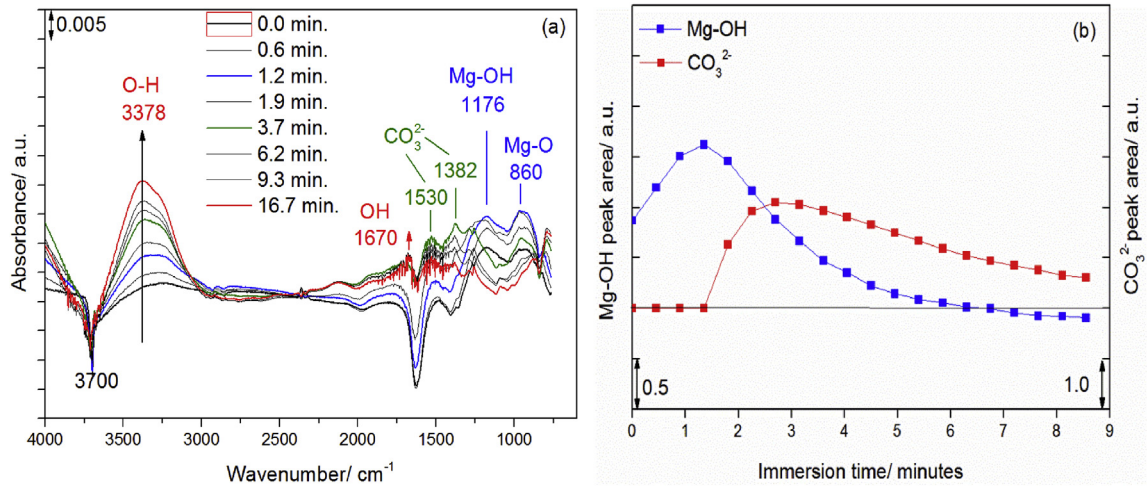

Fig. 2. (a) in situ ATR-FTIR spectra of magnesium exposed to demineralized water, (b) quantified Mg–OH and CO_3^{2-} peak areas as a function of immersion time.

previously [22].

3.2. In situ ATR-FTIR adsorption study of carboxylic corrosion inhibitors on magnesium

3.2.1. 2,5-Pyridinedicarboxylate (PDC)

Fig. 3 (a) presents the adsorption kinetics of neutralized PDC from aqueous solution using magnesium immersed in demineralized water as background. The spectrum shown in green illustrates the reference spectrum collected in absence of magnesium. Characteristic peaks in this reference spectrum positioned at 1577 and 1387 cm^{-1} are attributed to asymmetric and symmetric carboxylate stretching vibrations indicating the deprotonation of PDC acid at neutral and alkaline pH values ($pKa_1 = 2.35$, $pKa_2 = 4.64$ for 2,5-pyridinedicarboxylic acid at 20 °C and ionic strength 0.5) [75].

Above the reference spectrum the dynamic behaviour of native magnesium oxide in PDC solution is illustrated. Similar to the reference, asymmetric and symmetric carboxylate peaks positioned at 1584 and 1384 cm^{-1} appear during submersion of magnesium in PDC solution. Near the asymmetric carboxylate peak at 1584 cm^{-1} a second peak is noted assigned to OH-bending vibrations originating from bulk water. In addition, a new peak positioned at 1249 cm^{-1} assigned to Mg—OH bonds appear upon immersion. Similar to the kinetics of magnesium in demineralized water, this is associated to the formation of a hydroxylated magnesium oxide ($MgO/Mg(OH)_2$) layer. The quantified peak areas of the magnesium hydroxide (Mg—OH) and asymmetric and symmetric carboxylate (COO^-) peaks are plotted in Fig. 3 (b). After 1.5 min the Mg—OH peak area declines, while the carboxylate peak area rapidly increases. This implies that surface hydroxide end-groups are being consumed during the formation of magnesium-carboxylate bonds. After 3 min of immersion, both the asymmetric and symmetric carboxylate peaks and the Mg—OH peak reach a plateau. This indicates that chemisorption occurs rapidly, resulting in stable carboxylate bonds, which are able to resist replacement by water.

3.2.2. 3-Methylsalicylate (MSA)

The reference ATR-FTIR spectrum of MSA, shown in green in Fig. 4 (a), illustrates peaks at 1597, 1476 and 1395 cm^{-1}, attributed to carbon-carbon stretching vibrations in the aromatic ring, asymmetric and symmetric carboxylate stretching vibrations, respectively. The indication of carboxylate peaks in the reference spectrum again illustrate the deprotonated state of the inhibitor molecules at neutral and alkaline pH values ($pKa_1 = 2.82$, $pKa_2 = 14.6$ for 3-methylsalicylic acid at 25 °C and ionic strength 0.1 and 0 for Ka_1 and Ka_2, respectively) [76].

During the adsorption of MSA on magnesium, rapid peak formation is observed in the lower IR-frequency region, i.e. 1300-800 cm^{-1}. Similar to previously discussed kinetics of water and 2,5-

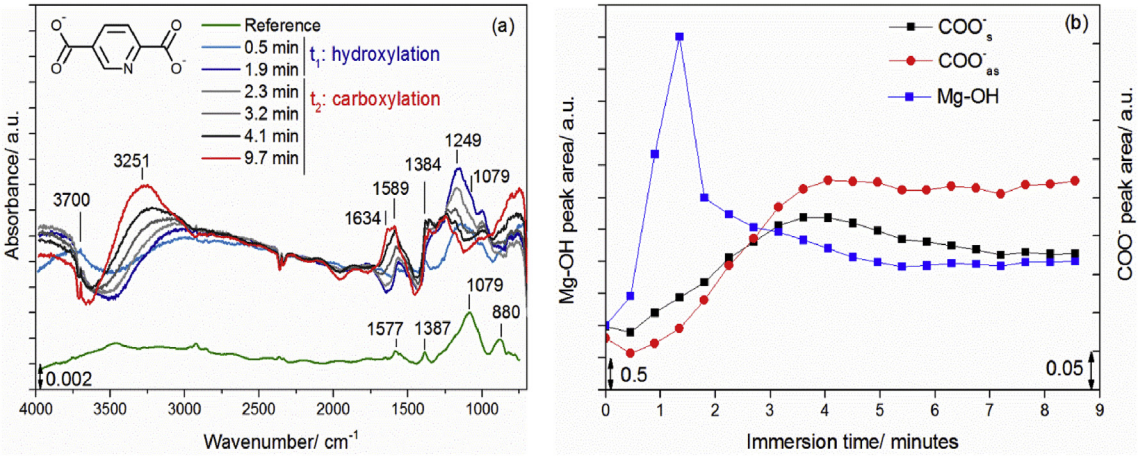

Fig. 3. (a) in situ ATR-FTIR adsorption spectra, (b) quantified Mg—OH and COO^- peak areas as a function of immersion time in PDC solution.

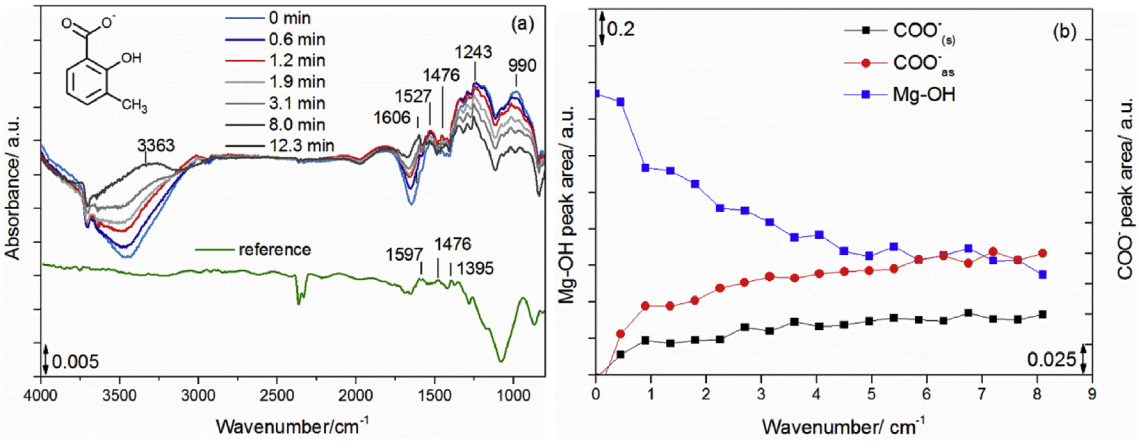

Fig. 4. (a) in situ ATR-FTIR adsorption spectra, (b) quantified Mg—OH and COO^- peak areas as a function of immersion time in MSA solution.

pyridinedicarboxylate, these broad bands, assigned to Mg–OH bonds, are related to surface hydroxylation reactions. Again a reduction of Mg–OH bonds is noted upon prolonged immersion. Similar to PDC, the reduction of Mg–OH is associated to the consumption of magnesium hydroxide end-groups during the formation of carboxylate bonds with MSA. This is confirmed by the growth of peaks at 1527 and 1476 cm^{-1}, assigned to asymmetric and symmetric carboxylate bond vibrations In addition, a new peak at 1606 cm^{-1} attributed to aromatic ring (C=C) stretching vibrations appears after 8 min of immersion in MSA solution. Furthermore, Fig. 4 (b) illustrates that both Mg–OH and COO^- peak areas keep evolving during prolonged immersion in MSA, whereas during immersion in PDC solution a plateau value was reached after 3 min of immersion in PDC solution.

3.2.3. Sodium salicylate (SS)

Fig. 5 (a) illustrates the adsorption kinetics of salicylate ($pKa_1 = 2.8$, $pKa_2 = 13.4$ for salicylic acid at 25 °C and ionic strength 0.1) [77] on $MgO/Mg(OH)_2$. Analogous to the reference spectrum, three distinct peaks instantaneously appear at 1607, 1470 and 1370 cm^{-1} attributed to aromatic ring vibrations, asymmetric and symmetric carboxylate stretch vibrations, respectively. The lack of distinct peaks in the lower wavenumber region (1000-1300 cm^{-1}) demonstrates the lack of surface hydroxylation. On the contrary, the negative peak observed at 1097 cm^{-1} refers to $Mg(OH)_2$ layer breakdown. This magnesium hydroxide consumption can be associated to the chelating abilities of salicylate forming soluble magnesium salicylate complexes (pK = 4.7) [78]. The formation of such magnesium salicylate complexes is evidenced by the growth of asymmetric and symmetric carboxylate peaks at 1470 and 1370 cm^{-1}, respectively. The quantified peak areas of these carboxylate peaks are illustrated in Fig. 5 (b). It can be seen that magnesium-carboxylate complexes are formed rapidly, whereas the Mg–OH bonds associated to the $MgO/Mg(OH)_2$ layer instantaneously decline.

3.2.4. Fumarate (FA)

The green curve in Fig. 6 (a) presents the reference ATR-FTIR spectrum of FA in solution in absence of magnesium. Two distinct peaks positioned at 1564 and 1373 cm^{-1} attributed to asymmetric and symmetric carboxylate bonds are noted, which again illustrates its deprotonated state in the respective solution ($pKa_1 = 2.85$, $pKa_2 = 4.1$ for fumaric acid at 25 °C and ionic strength 0.1)[77]. However, in situ ATR-FTIR data does not reveal spectral features correlated to the chemisorption of FA. On the other hand, immediate growth of broad peaks in the low IR-region indicates the formation of a hydroxylated layer. Simultaneously obtained EIS spectra, shown in Fig. 6 (b), demonstrate increasing impedance values upon immersion. However, the increase of impedance is minor compared to the other inhibitor solutions. Therefore, the

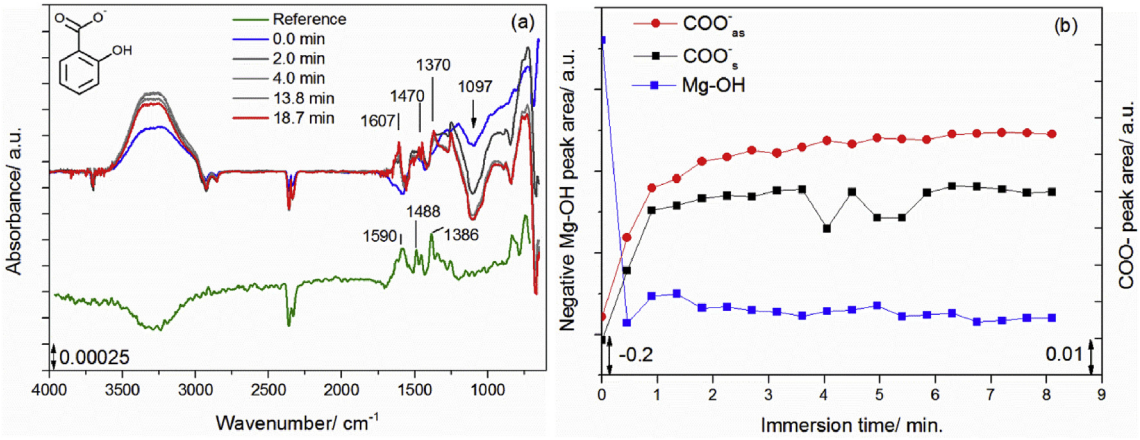

Fig. 5. (a) in situ ATR-FTIR adsorption spectra, (b) quantified Mg–OH and COO^- peak areas as a function of immersion time in SS solution.

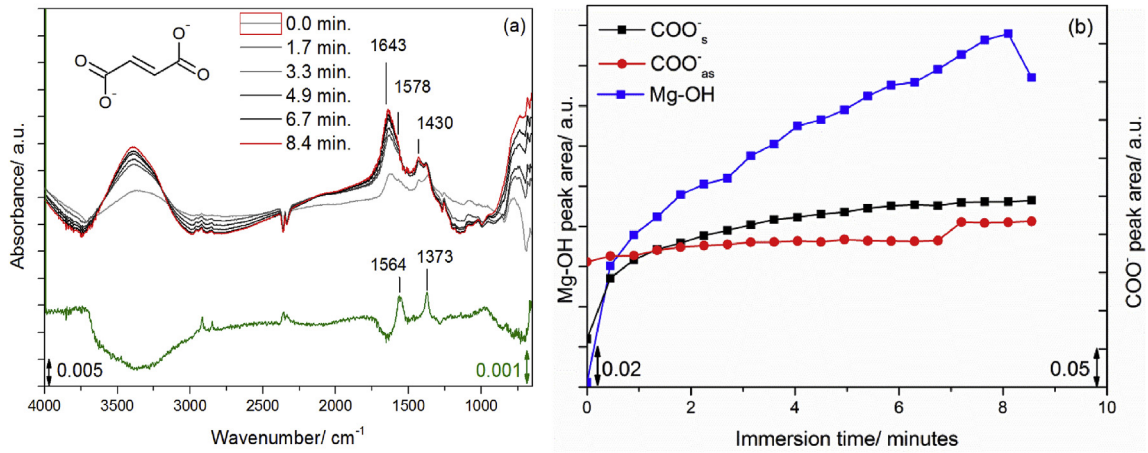

Fig. 6. (a) in situ ATR-FTIR adsorption spectra, (b) quantified Mg–OH and COO- peak areas as a function of immersion time in FA solution.

protective properties of the established hydroxylated layer are suggested to be limited.

3.3. EIS study of magnesium immersed in carboxylic corrosion inhibitor solutions

The Bode plots shown in Fig. 7, present the EIS data recorded simultaneously with the ATR-FTIR measurements shown in Figs. 3–6. It is noted that the impedance modulus increases instantaneously during submersion of magnesium in the inhibitor solutions. Similar also the phase angle increases and broadens during submersion of in the inhibitor solutions, which is associated to the formation of a protective layer, as suggested by the in situ ATR-FTIR measurements.

The EIS data obtained during submersion in PDC, MSA, SS and FA solution are highly scattered at low frequencies (10^{-1} - 10° Hz) due to fast dissolution of magnesium substrate leading to non-stationarities. Therefore, EIS fitting has been performed in the frequency region 10°–10^{4} Hz. Within this region one timeconstant can be distinguished from the phase angle plots associated to the formation of a protective film. Consequently, the hydroxylated MgO(/$Mg(OH)_2$ layer and its chemisorbed carboxylate species are considered as one protective film. The protective properties of this dynamic film are being quantified by fitting the EIS data using an electrical equivalent circuit (EEC) containing one timeconstant. This EEC is illustrated in Fig. 8, and is composed of the electrolyte resistance R_{el}, followed by the time-constant associated to the formed protective film (f), with R_f representing the film resistance and CPE_f being the constant phase element describing the capacitance of the film. It is very likely, that a second time-constant representative for electrochemical processes at the $MgO/Mg(OH)_2$ – electrolyte interface exists at lower frequencies. However, due to largely scattered EIS data (caused by non-stationarity) these processes are not quantified by EIS fitting. In the case of sodium salicylate, shown in Fig. 7(e–f), the phase angle values obtained between 10^{4} - 10^{2} Hz exceeds -90°. Because of this unusual feature, reliable fitting could not be performed in the frequency region of interest. Therefore, no fitting results are displayed in the Bode plots measured during immersion in sodium salicylate, shown in Fig. 7(e–f). Moreover, the associated decrease of surface area eventually (in ca. 5 min) leads to the loss of magnesium layer, which is in line with the ATR-FTIR – EIS data shown in Fig. 5, where sodium saliclyate was described as a corrosion accelerator rather than a corrosion inhibitor.

The resulting fitting values associated to the protective properties of the $MgO/Mg(OH)_2$ film and its chemisorbed carboxylate species are given in Table 2.

The evolution of quantified capacitance properties (Q and n) associated to film formation during submersion in inhibitor solution are shown in Fig. 9(a) and (b), respectively. All carboxylic inhibitor solutions are shown to reduce the film CPE Q value. These reducing CPE Q values imply reduced polarizability of the formed film indicating increased protective properties during prolonged immersion in the respective inhibitor solutions [79,80]. From Fig. 9 (a), reducing CPE Q values are noted in the following order: FA > PDCA > MSA. Therefore, the film formed during submersion of magnesium in MSA solution has the lowest polarizability and thus the highest protective properties. In line with these results, Fig. 9 (b) demonstrates increasing n-values during submersion of MSA approaching the ideal capacitor during prolonged immersion of magnesium. Conversely, the n-values are shown to decrease upon immersion of magnesium in FA and PDC. Whereas the values of FA remain close to its initial values, the decrease is highly pronounced in the case of PDC. Therefore, the formed film in PDC solution is suggested to be less homogeneous compared to FA and MSA.

The resulting film resistance (R_f) of $MgO/Mg(OH)_2$ evolution is shown in Fig. 10. Increasing film resistances with prolonged immersion times are observed in following order: MSA > PDC > FA. These results are in accordance with those reported by Maltseva et al. who attributed the higher barrier properties during immersion in MSA compared to PDC and FA to the formation of a dense and stable $MgO/Mg(OH)_2$ layer [81,82]. PDC gives the second best inhibiting efficiency, although a delay time can be noted. The slightly better performance of PDC compared to FA is expected to relate to additional surface interactions with the pyridine ring electrons (π-interactions) and nitrogen atom. Finally, SS shows the poorest protection capacities which was attributed to the formation of soluble magnesium salicylate complexes. Because of its chelating capacities, salicylate was shown to act as a corrosion accelerator for high purity magnesium, which is reflected in the electrochemical measurements as rapid dissolution of magnesium disconnecting the electrochemical cell. Because of this, film resistance values for magnesium in the presence of SS are not shown in Fig. 10.

From Fig. 10, it is inferred that increased film resistance values are noted after a delay time of approximately 3 min. The ATR-FTIR results presented in Fig. 11 (a) demonstrate that within this time lag oxide hydroxylation takes place. The growth of a hydroxylated $MgO/Mg(OH)_2$ layer takes place instantaneously, reaching a maximum intensity within less than 2 min. Thereafter, the hydroxide concentration reduces, which is associated to hydroxide consumption required for carboxylate bond formation as indicated by the increasing carboxylate peak areas shown in Fig. 11 (b). The strong Mg–OH peak area decay noted for PDC relates to the deprotonation of the second acid group of PDC [81,82]. This is in line with the higher asymetrica carboxylate peak area observed for PDC, referring to a two-end adsorption, where both carboxylate groups coordinate to magnesium cations at the $MgO/Mg(OH)_2$ surface. Therefore, the increased film resistance, shown in Fig. 10 can be attributed to two surface phenomena, being the formation of a $MgO/Mg(OH)_2$ layer, as well as the chemisorption of carboxylic compounds.

3.4. Orientation analysis using s- and p-polarized IR-light

To further investigate the binding mechanism of carboxylic compounds on the evolving $MgO/Mg(OH)_2$ layer, orientation analysis of the chemisorbed carboxylate species has been performed using p- and s-polarized IR-light. The use of p-polarized light (90°) probes molecular vibrations with their transition dipole moment perpendicular to the surface, whereas s-polarized light (0°) probes molecular vibrations with their transition dipole moment in plane with the surface.

In situ ATR-FTIR spectra of PDC, MSA and SS obtained using p-polarized IR-light are shown in Fig. 12(a–c) respectively. Spectral features are limited to negative bands characteristic for species present in the background. Therefore, chemisorption of these aromatic compounds could not be monitored using p-polarized IR-light. On the other hand, FA, presented in Fig. 12 (d), clearly demonstrates two distinct peaks positioned at 1570 and 1366 cm^{-1} attributed to asymmetric and symmetric carboxylate bonds respectively. The separation of both peaks by 181 cm^{-1} suggests a bridging bidentate carboxylate coordination [83]. Additionally, their high sensitivity for p-polarized IR-light indicates that carboxylate bonds are highly oriented perpendicular to the magnesium oxide surface. Furthermore, it can be seen that only MSA has positive OH bands at 3560 cm^{-1}. This observation is in line with the previously discussed stabilization of the hydroxylated $MgO/Mg(OH)_2$ film by MSA.

In situ ATR-FTIR spectra of PDC, MSA and SS obtained using s-polarized IR-light are shown in Fig. 13(a–c) respectively. For PDC

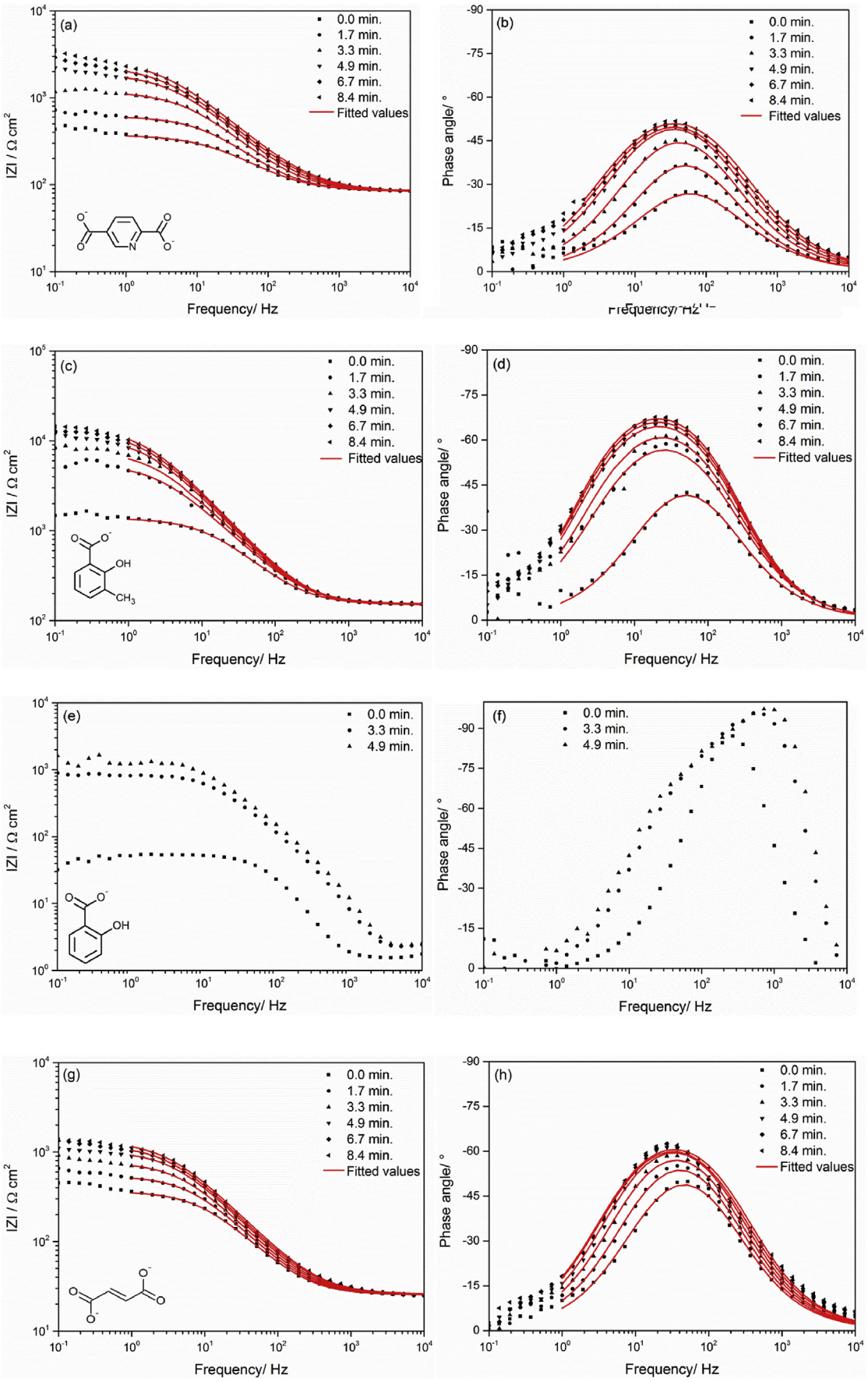

Fig. 7. Bode modulus of magnesium immersed in (a) PDC, (c) MSA, (e) SS and (g) FA and phase angle plots of magnesium immersed in (b) PDC, (d) MSA, (f) SS and (h) FA.

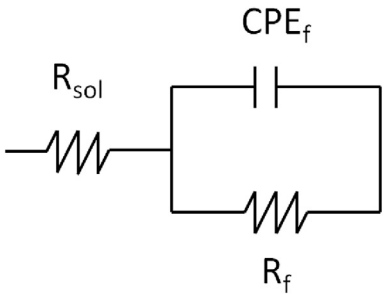

Fig. 8. Proposed equivalent electrical circuit used for fitting EIS spectra obtained in the 10^0–10^4 Hz region during immersion of magnesium in the inhibitor solutions PDC, MSA and FA.

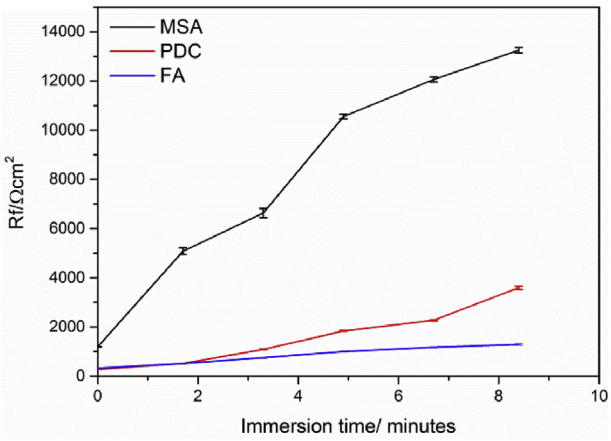

Fig. 10. Film resistance evolution during immersion in the respective inhibitor solutions.

and SS hydroxylation (indicated in blue) followed by carboxylation (indicated in red) is observed using s-polarized light, which is similar to the trends observed using non-polarized IR-light. This once again illustrates that the hydroxylated surface is not stable in the respective solutions. On the other hand, in situ ATR-FTIR adsorption spectra of MSA, shown in Fig. 13 (b), demonstrates simultaneous hydroxylation and carboxylation. Both processes are shown to be stable confirming the capability of MSA to stabilize formed hydroxide layers. Next to carboxylate peaks, also aromatic ring vibrations (indicated in green) are excited using s-polarized IR-light. This together with the absence of vibrational bonds using p-

Table 2
Fitting parameters of EIS spectra obtained in ATR-FTIR electrochemical cell during adsorption of magnesium in the respective inhibitor solutions.

Time/min	R_{sol}/Ωcm [2]	Q (CPE$_f$)/μSs^n cm^{-2}	n (CPE$_f$)	R_f/Ωcm [2]	χ [2]
2,5-PDC					
0.0	83 ± 0.5	85.6 ± 3.0	0.75 ± 0.01	287 ± 3	1.6×10^{-3}
1.7	85 ± 0.3	50.3 ± 1.4	0.80 ± 0.01	518 ± 4	7.0×10^{-4}
3.3	85 ± 0.6	42.8 ± 1.3	0.79 ± 0.01	1092 ± 17	1.1×10^{-3}
4.9	84 ± 0.6	39.3 ± 0.9	0.77 ± 0.01	1839 ± 23	1.1×10^{-3}
6.7	83 ± 0.6	39.0 ± 0.8	0.76 ± 0.01	2275 ± 27	8.9×10^{-4}
8.4	82 ± 0.5	32.5 ± 0.6	0.75 ± 0.01	3595 ± 67	6.6×10^{-4}
3-MSA					
0.0	150 ± 0.5	20.2 ± 0.4	0.83 ± 0.01	1192 ± 8	1.2×10^{-3}
1.7	150 ± 1.3	16.3 ± 0.5	0.83 ± 0.01	5081 ± 136	2.6×10^{-3}
3.3	150 ± 1.1	13.6 ± 0.3	0.85 ± 0.01	6630 ± 189	3.0×10^{-3}
4.9	151 ± 0.6	11.7 ± 0.1	0.86 ± 0.01	10,551 ± 94	4.3×10^{-4}
6.7	153 ± 0.6	10.6 ± 0.1	0.87 ± 0.01	12,062 ± 105	3.9×10^{-4}
8.4	153 ± 0.5	9.8 ± 0.1	0.88 ± 0.01	13,250 ± 112	3.7×10^{-4}
FA					
0.0	25 ± 0.2	90.1 ± 2.7	0.85 ± 0.01	330 ± 4	1.7×10^{-3}
1.7	26 ± 0.2	80.5 ± 2.9	0.85 ± 0.01	516 ± 11	2.3×10^{-3}
3.3	26 ± 0.3	74.4 ± 2.7	0.85 ± 0.01	754 ± 20	2.8×10^{-3}
4.9	26 ± 0.3	66.8 ± 2.2	0.85 ± 0.01	999 ± 20	3.4×10^{-3}
6.7	26 ± 0.3	66.4 ± 2.2	0.84 ± 0.01	1173 ± 26	3.7×10^{-3}
8.4	26 ± 0.3	62.0 ± 2.0	0.84 ± 0.01	1291 ± 30	3.7×10^{-3}

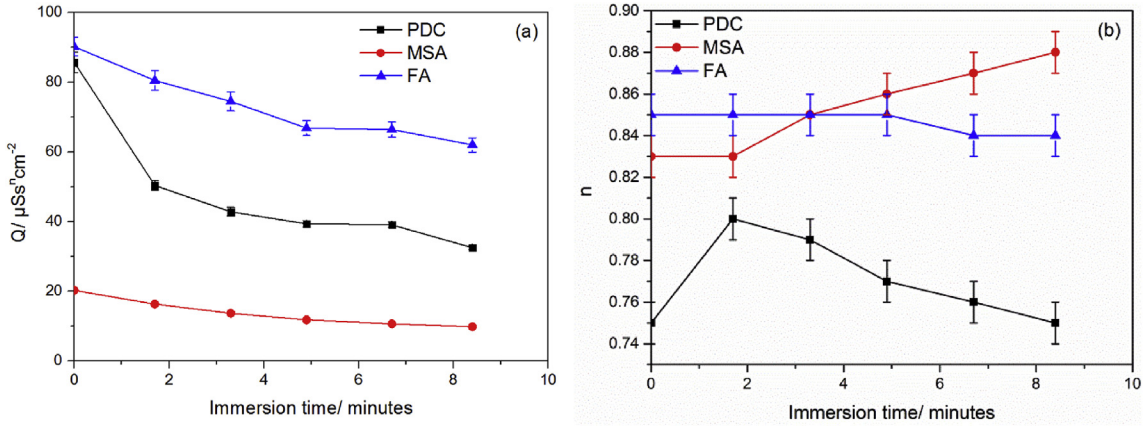

Fig. 9. Inhibitor film CPE fitting values (a) Q and (b) n.

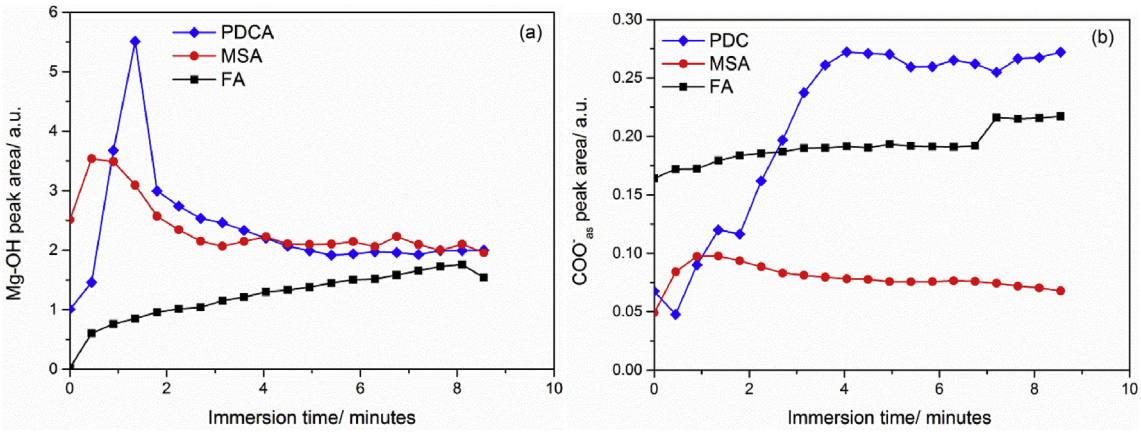

Fig. 11. In situ ATR-FTIR results (a) Mg–OH peak and (b) asymmetric carboxylate peak area evolution during immersion in PDC, MSA and FA solution.

polarized IR-light, indicates that aromatic compounds are oriented in plane with the $MgO/Mg(OH)_2$ surface. The in plane orientation observed for aromatic compounds suggest that strong interactions are taking place between metal oxide and π-electrons of the aromatic ring [84]. Conversely, chemisorption of FA is not elucidated using s-polarized IR-light, which confirms the highly oriented bridging bidentate coordination perpendicular to the magnesium oxide surface.

Using polarized IR-light, ATR-FTIR revealed two adsorption orientations distinguishing aliphatic from aromatic structures. Fig. 14 (a) depicts FA with its hydrocarbon backbone in plane with the $MgO/Mg(OH)_2$ surface but with a transition dipole of the carboxylate bonds perpendicular to the substrate explaining its sensitivity for p-polarized IR-light. Conversely, PDC, presented in Fig. 14 (b), shows an orientation of both the hydrocarbon backbone with aromatic ring as well as the transition dipole moment of the

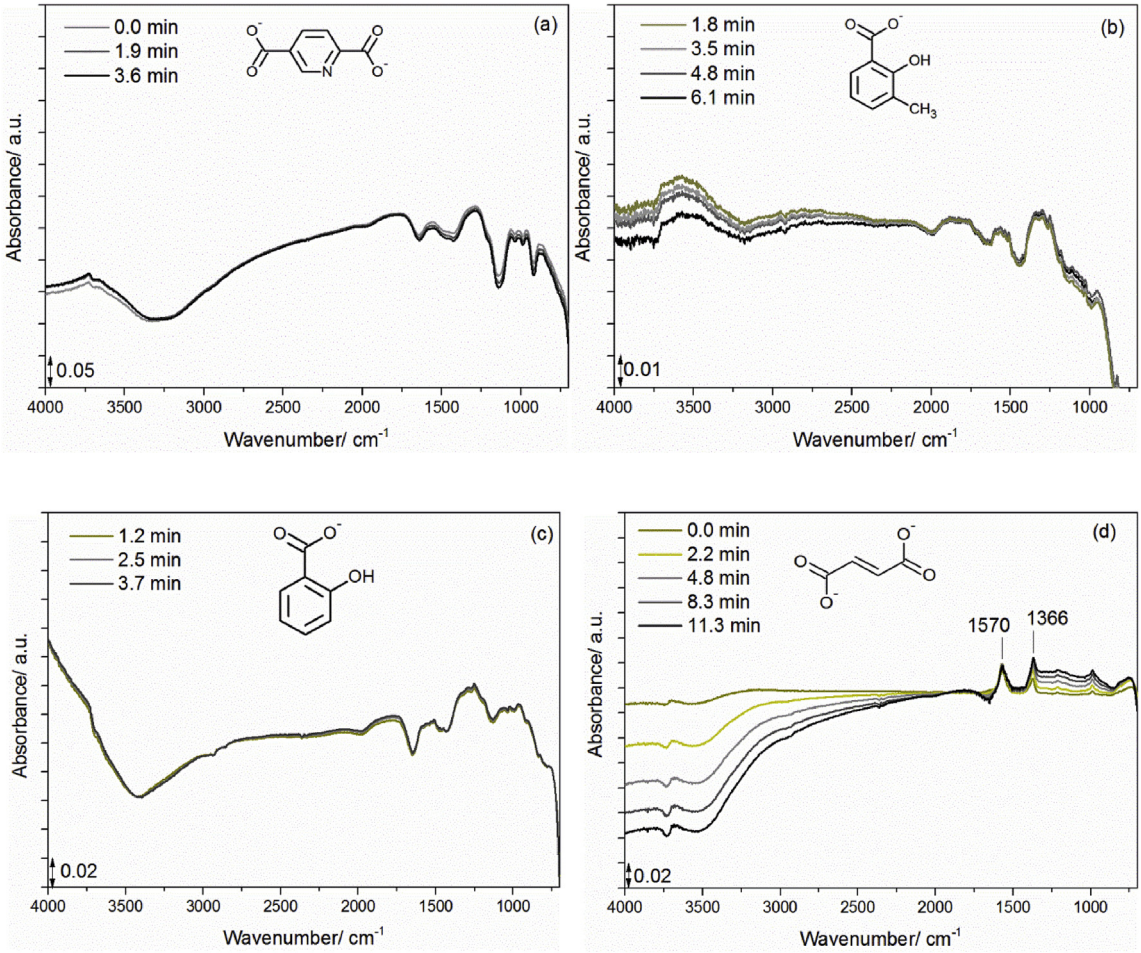

Fig. 12. P-polarized ATR-FTIR spectra of magnesium during immersion in inhibitor solutions containing (a) PDC, (b) MSA, (c) SS and (d) FA.

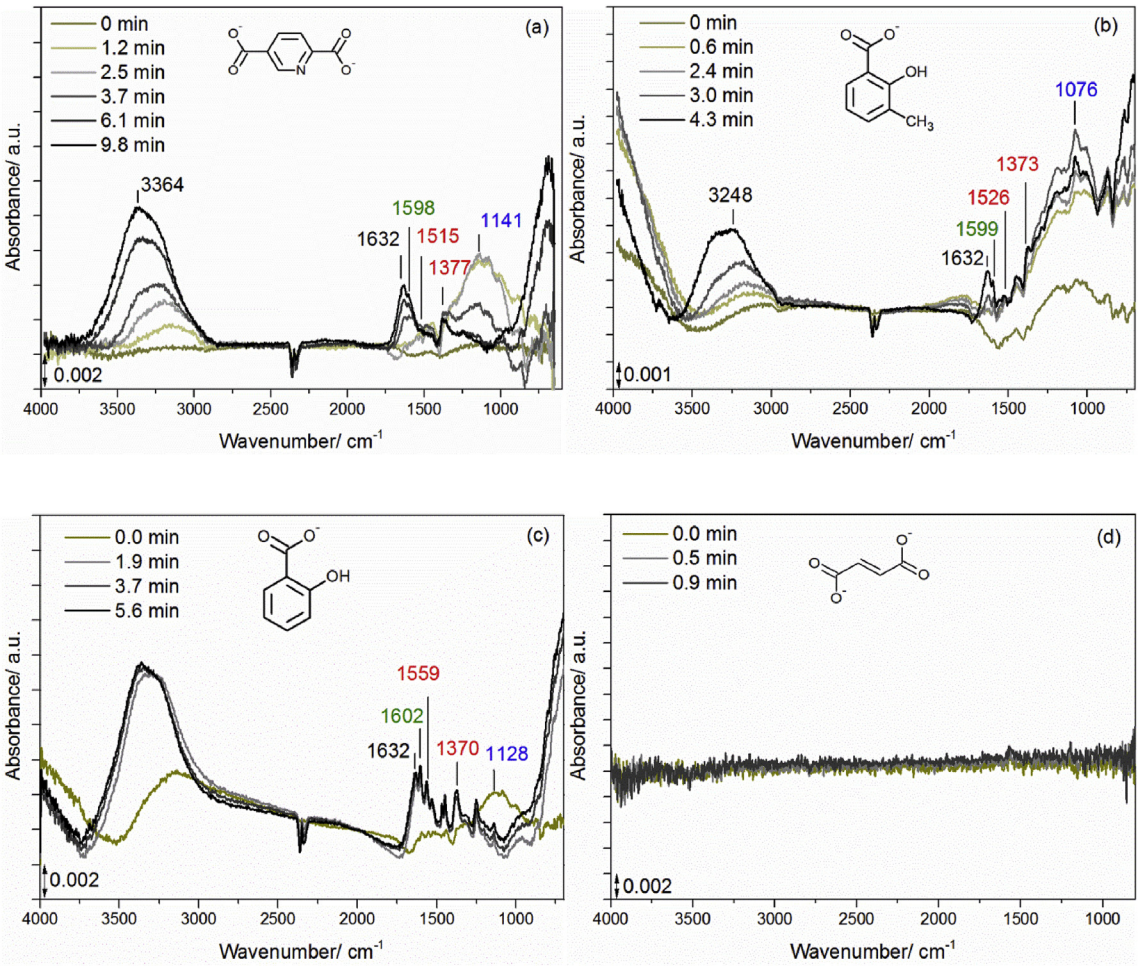

Fig. 13. S-polarized ATR-FTIR spectra of magnesium during immersion in inhibitor solutions containing (a) PDC, (b) MSA, (c) SS and (d) FA.

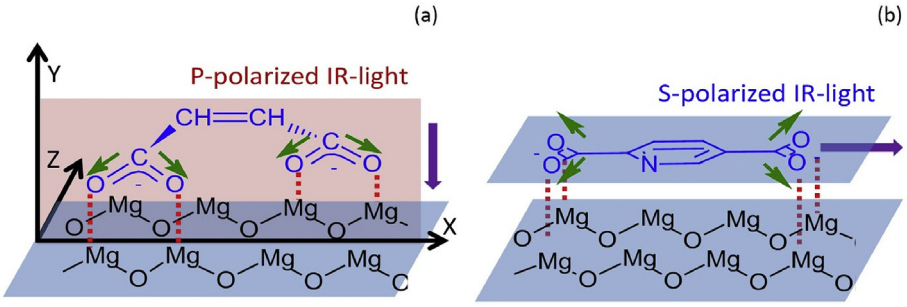

Fig. 14. Graphical representation transition dipole moments carboxylates bonds and the corresponding polarized IR-light beams used to probe them; (a) FA, (b) PDC.

carboxylate bonds in plane with the MgO/$Mg(OH)_2$ surface. In line with their sensitivity for s-polarized IR-light, the latter representation is assumed to also apply for SS and MSA. The graphical representation given in Fig. 14 also illustrates why surface hydroxylation processes are more distinct in FTIR spectra using s-polarized IR-light compared to p-polarized IR-light as shown in Figs. 12 and 13, respectively.

3.5. Adsorption study using DFT calculations

For a more comprehensive understanding of the adsorption behaviour of the investigated inhibitor molecules at the MgO/$Mg(OH)_2$ interface, density functional theory (DFT) computations were performed. Fig. 15 presents the two orientations upright and flat to the molecular symmetry plane being perpendicular and in plane with the magnesium (hydr)oxide surface, respectively. Monodentate and bidentate chelating starting structures always relaxed to one of these orientations. From the obtained adsorption energies, preferential orientation of the molecules in plane (flat) with the partially hydroxylated MgO (100) surface is demonstrated for a surface coverage $\theta = 0.25$ monolayers (ML). The highest adsorption energy is obtained for PDC. However, due to a varying number of co-adsorbed hydrogen atoms, adsorption energies from inhibitors yielding different numbers of carboxylate groups are not

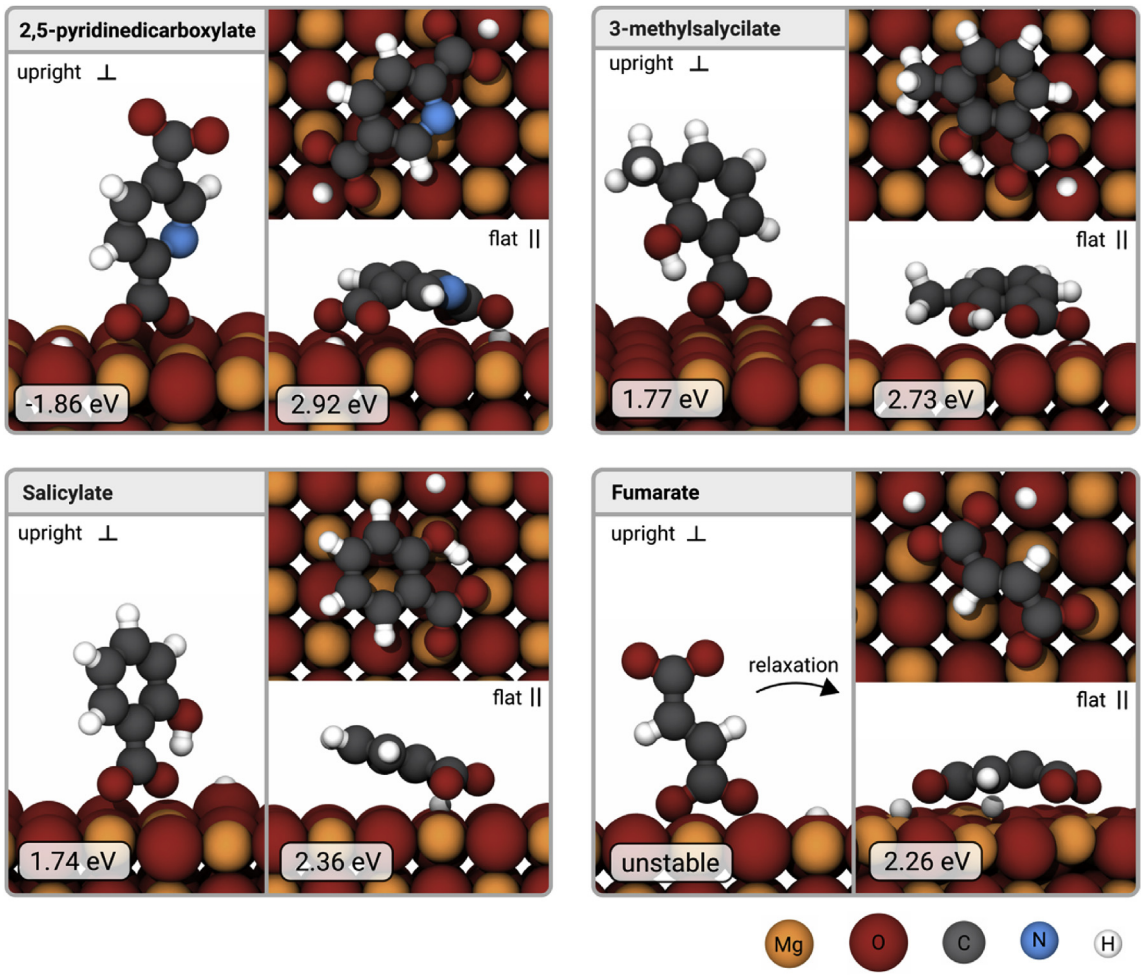

Fig. 15. The DFT-computed adsorption structures of the investigated inhibitor molecules including their respective adsorption energies on the partially hydroxylated MgO(100) surface for a coverage $\theta = 0.25$ ML. The structures are categorized into upright and flat, according to the orientation of the molecular symmetry plane relative to the substrate.

directly comparable. Yet comparing dicarboxylic acids; PDC (E_{ads} = 2.92 eV) and FA (E_{ads} = 2.26 eV) and the monocarboxylic acids; MSA (E_{ads} = 2.73 eV) and SS (E_{ads} = 2.36 eV) reveals that molecular structures with additional hetero-atoms (nitrogen atom or hydroxyl groups respectively) increase the adsorption energy. As a consequence, it is expected that also hetero-atoms are involved in the interaction with magnesium (hydr)oxide. In addition, based on the preferred in plane orientation, it is inferred that the two carboxylic acid groups of the dicarboxylic acids (PDC and FA) are involved in the adsorption, leading to a two-end adsorption mechanism. These results are in line with the ATR-FTIR output presented in Fig. 14.

4. Conclusions

Surface phenomena, including both hydration and dissolution, as well as inhibitor chemisorption mechanisms were followed in situ using the integrated ATR-FTIR – EIS setup. Submersion of magnesium into aqueous solution was shown to induce two surface processes: (1) surface hydroxylation reactions forming a MgO/$Mg(OH)_2$ layer and (2) chemisorption phenomena. In demineralized water dissolved CO_2 was shown to chemisorb to the MgO/$Mg(OH)_2$ layer, but the formed carbonate complexes were shown to be unstable. Conversely, when carboxylic acid compounds were added to the aqueous solution, stable magnesium-carboxylate bonds were formed, which were able to resist replacement by water. Orientation analysis using polarized IR-light showed the transition dipoles of carboxylate bonds established with aromatic compounds are in plane with the surface, whereas those observed for aliphatic FA are oriented perpendicular to the surface. Supportive DFT calculations confirmed the in-plane orientation of aromatic compounds allowing for π-interactions between the aromatic ring and MgO/$Mg(OH)_2$. Also the hydrocarbon backbone of FA, oriented in plane with the surface, allowing for a two-end adsorption. In addition DFT indicated increased adsorption energies when additional hetero-atoms (Being N or OH) were added to the molecular structure. Quantification of the film resistances at consecutive immersion times gave insights in the protective properties of the formed film consisting of a MgO/$Mg(OH)_2$ layer with chemisorbed carboxylate species. MSA showed the highest inhibiting performance which was attributed to the stabilization of the MgO/$Mg(OH)_2$ layer. On the other hand, SS was shown to act as a corrosion accelerator dissolving MgO/$Mg(OH)_2$. Hence, combined use of ATR-FTIR and EIS highlighted the predominant role of the MgO/$Mg(OH)_2$ layer in terms of inhibitor performance. Therefore, the integrated ATR-FTIR – EIS setup is proposed as a highly valuable tool to simultaneously describe inhibiting mechanisms and efficiency. Further development of the proposed in situ screening methodology is recommended. The first recommendation on further development of the integrated ATR-FTIR –EIS methodology

for corrosion inhibitor screening relates to the low quality EIS data in the low frequency region. For rapid evolving systems such as immersion of magnesium substrate in corrosive environments, it is suggested to combine ATR-FTIR Kretschmann measurements with multisine EIS. Two major advantages of multisine EIS over classical EIS are firstly, it may significantly reduce the analysis time which is beneficial for the stationarity requirement of EIS, since this is challenging for rapid evolving systems and secondly, if non-stationarities or non-linearity's occur during the analysis time, they can be quantified using odd random phase analysis. The second recommendation relates to the translation of pure model magnesium substrates, to the inhibition mechanisms occurring on magnesium alloys used in engineering applications. The inhibiting efficiencies demonstrated in this work using pure magnesium substrates were in accordance to those reported previously on as-cast commercial purity magnesium (CP−Mg342) and high purity magnesium (HP−Mg51) [81,82]. Mimicking such alloys by means of thermal evaporation would be highly interesting to gain more fundamental insights on the role of impurities on corrosion inhibition mechanisms.

Declaration of competing interest

The authors declare that they have no known competing financial interests or personal relationships that could have appeared to influence the work reported in this paper.

CRediT authorship contribution statement

L.I. Fockaert: Writing - original draft. **T. Würger:** Investigation, Data curation, Formal analysis, Methodology. **R. Unbehau:** Investigation, Writing - review & editing. **B. Boelen:** Writing - review & editing. **R.H. Meißner:** Writing - review & editing. **S.V. Lamaka:** Conceptualization, Writing - review & editing. **M.L. Zheludkevich:** Writing - review & editing. **H. Terryn:** Writing - review & editing. **J.M.C. Mol:** Writing - review & editing.

Acknowledgements

This research was carried out under project number F81.3.13509 in the framework of the Partnership Program of the Materials innovation institute M2i (www.m2i.nl) and the Foundation for Fundamental Research on Matter (FOM), which is part of the Netherlands Organisation for Scientific Research NWO (www.nwo.nl). R.U. acknowledges funding by the German Research Foundation through the GRK2154. R.M. gratefully acknowledges funding by the Deutsche Forschungsgemeinschaft (DFG, German Research Foundation) − project number 192346071 - SFB 986, and project number 390794421 - GRK 2462. S.L. acknowledges funding by the Helmholtz Zentrum Geesthacht in frame of MMDi IDEA project. Martin Wolf from Metallic Biomaterials of Helmholtz Zentrum Geesthacht is acknowledged for providing the magnesium substrate used for PVD deposition. Dr. Christian Feiler from Magnesium Innovation Center of Helmholtz Zentrum Geesthacht is acknowledged for discussion on orientation of studied carboxylates. Dr. Majid Sababi formerly from TUDelft is acknowledged for preliminary ATR-FTIR-EIS measurements on UHP Mg.

Appendix A. Supplementary data

Supplementary data to this article can be found online at https://doi.org/10.1016/j.electacta.2020.136166.

References

[1] T.J. Harvey, F.C. Walsh, A.H. Nahlé, A review of inhibitors for the corrosion of transition metals in aqueous acids, J. Mol. Liq. 266 (2018) 160−175.
[2] J. Yang, C. Blawert, S.V. Lamaka, K.A. Yasakau, L. Wang, D. Laipple, M. Schieda, S. Di, M.L. Zheludkevich, Corrosion inhibition of pure Mg containing a high level of iron impurity in PH neutral NaCl solution, Corrosion Sci. 142 (2018) 222−237.
[3] M. Esmaily, J.E. Svensson, S. Fajardo, N. Birbilis, G.S. Frankel, S. Virtanen, R. Arrabal, S. Thomas, L.G. Johansson, Fundamentals and advances in magnesium alloy corrosion, Prog. Mater. Sci. 89 (2017) 92−193.
[4] B.L. Mordike, T. Ebert, Magnesium: properties - applications - potential, Mater. Sci. Eng. 302 (2001) 37−45.
[5] M. Meeusen, P. Visser, L. Fernández Macía, A. Hubin, H. Terryn, J.M.C. Mol, The use of odd random phase electrochemical impedance spectroscopy to study lithium-based corrosion inhibition by active protective coatings, Electrochim. Acta 278 (2018) 363−373.
[6] P. Visser, M. Meeusen, Y. Gonzalez-Garcia, H. Terryn, J.M.C. Mol, Electrochemical evaluation of corrosion inhibiting layers formed in a defect from lithium-leaching organic coatings, J. Electrochem. Soc. 164 (7) (2017) C396−C406.
[7] D. Snihirova, S.V. Lamaka, P. Taheri, J.M.C. Mol, M.F. Montemor, Comparison of the synergistic effects of inhibitor mixtures tailored for enhanced corrosion protection of bare and coated AA2024-T3, Surf. Coating. Technol. 303 (2016) 342−351.
[8] S.V. Lamaka, B. Vaghefinazari, D. Mei, R.P. Petrauskas, D. Höche, M.L. Zheludkevich, Comprehensive screening of Mg corrosion inhibitors, Corrosion Sci. 128 (2017) 224−240.
[9] S.V. Lamaka, M.L. Zheludkevich, K.A. Yasakau, M.F. Montemor, M.G.S. Ferreira, High effective organic corrosion inhibitors for 2024 aluminium alloy, Electrochim. Acta 52 (25) (2007) 7231−7247.
[10] C. Feiler, D. Mei, B. Vaghefinazari, W. Tim, R.H. Meißner, B.J. C, B.J.C. Luthringer-feyerabend, D.A. Winkler, M.L. Zheludkevich, S.V. Lamaka, In silico screening of modulators of magnesium dissolution, Corrosion Sci. 163 (2020) 108245−108253.
[11] M. Esmaily, J.E. Svensson, S. Fajardo, N. Birbilis, G.S. Frankel, S. Virtanen, R. Arrabal, S. Thomas, L.G. Johansson, Fundamentals and advances in magnesium alloy corrosion, Prog. Mater. Sci. 89 (2017) 92−193.
[12] T. Rabizadeh, S.K. Asl, Casein as a natural protein to inhibit the corrosion of mild steel in HCl solution, J. Mol. Liq. 276 (2019) 694−704.
[13] J.V. Nardeli, C.S. Fugivara, M. Taryba, E.R.P. Pinto, M.F. Montemor, Tannin : a natural corrosion inhibitor for aluminum alloys, Prog. Org. Coating 135 (2019) 368−381.
[14] D.S. Chauhan, A.M. Kumar, M.A. Quraishi, Hexamethylenediamine functionalized glucose as a new and environmentally benign corrosion inhibitor for copper, Chem. Eng. Res. Des. 150 (2019) 99−115.
[15] C. Örnek, C. Leygraf, J. Pan, On the Volta potential measured by SKPFM−fundamental and practical aspects with relevance to corrosion science, Corrosion Eng. Sci. Technol. 54 (3) (2019) 185−198.
[16] P.J. Denissen, S.J. Garcia, Reducing subjectivity in EIS interpretation of corrosion and corrosion inhibition processes by in-situ optical analysis, Electrochim. Acta 293 (2019) 514−524.
[17] S. Li, Intelligent Coatings for Corrosion Control, Chapter 20: Monitoring Corrosion Using Vibrational Spectroscopic Techniques, Elsevier Inc., 2015.
[18] A. You, M.A.Y. Be, I. In, Periodic trends in the bonding and vibrational Coupling : pyridine interacting with transition metals and noble metals studied by surface-enhanced Raman spectroscopy and density-functional theory, J. Chem. Phys. 119 (2003) 1701−1709.
[19] J.L. Yao, B. Ren, Z.F. Huang, P.G. Cao, R.A. Gu, Z. Tian, Extending surface Raman spectroscopy to transition metals for practical applications IV, A Study on Corrosion Inhibition of Benzotriazole on Bare Fe Elect. 48 (2003) 1263−1271.
[20] S. Huo, J. He, L. Chen, J. Fang, Adsorption configuration of sodium 2-quinoxalinecarboxylate on iron Substrate : investigation by in situ SERS , XPS and theoretical calculation, Spectrochim. Acta Part A Mol. Biomol. Spectrosc. 156 (2016) 123−130.
[21] E.M. Sherif, R.M. Erasmus, J.D. Comins, In situ Raman spectroscopy and electrochemical techniques for studying corrosion and corrosion inhibition of iron in sodium chloride solutions, Electrochim. Acta 55 (11) (2010) 3657−3663.
[22] A. Maltseva, V. Shkirskiy, G. Lefèvre, P. Volovitch, Effect of PH on Mg(OH)2 film evolution on corroding Mg by in situ kinetic Raman mapping (KRM), Corrosion Sci. 153 (2019) 272−282.
[23] P.R. Griffiths, J.A. de Haseth, Fourier Transform Infrared Spectrometry, second ed., John Wiley & Sons, Inc., 2007.
[24] L. Philippe, C. Sammon, S.B. Lyon, J. Yarwood, An FTIR/ATR in situ study of sorption and transport in corrosion protective organic coatings 1. Water sorption and the role of inhibitor anions, Prog. Org. Coating 49 (4) (2004) 302−314.
[25] X.H. Guan, Q. Liu, G.H. Chen, C. Shang, Surface complexation of condensed phosphate to aluminum hydroxide: an ATR-FTIR spectroscopic investigation, J. Colloid Interface Sci. 289 (2) (2005) 319−327.
[26] Vinogradov, A. P.; Dorofeenko, A. V; Pukhov, A. A.; Lisyansky, A. A. Exciting Surface Plasmon Polaritons in the Kretschmann Configuration by Light Beam. 1−23.
[27] S.A. Maier, Plasmonics: Fundamentals and Applications, Springer Science &

Business Media, 2007.
[28] M. Öhman, D. Persson, An integrated in situ ATR-FTIR and EIS set-up to study buried metal − polymer interfaces exposed to an electrolyte solution, Electrochim. Acta 52 (2007) 5159−5171.
[29] P. Taheri, J.H.W. De Wit, H. Terryn, J.M.C. Mol, In situ study of buried metal-polymer interfaces exposed to an aqueous solution by an integrated ATR-FTIR and electrochemical impedance spectroscopy system, J. Phys. Chem. C 117 (40) (2013) 20826−20832.
[30] S. Pletincx, J.M.C. Mol, H. Terryn, A. Hubin, T. Hauffman, An in situ spectro-electrochemical monitoring of aqueous effects on polymer/metal oxide interfaces, J. Electroanal. Chem. 848 (2019), 113311−11327.
[31] H. Behzadi, A. Forghani, Correlation between electronic parameters and corrosion inhibition of benzothiazole derivatives- NMR parameters as important and neglected descriptors, J. Mol. Struct. 1131 (2017) 163−170.
[32] H. Ashassi-sorkhabi, S. Moradi-alavian, M.D. Esrafili, A. Kazempour, Hybrid sol-gel coatings based on silanes-amino acids for corrosion protection of AZ91 magnesium Alloy : electrochemical and DFT insights, Prog. Org. Coating 131 (2019) 191−202.
[33] H. Behzadi, P. Roonasi, M. Jafar, S. Manzetti, M.D. Esrafili, I.B. Obot, M. Yousefvand, S.M. Mousavi-khoshdel, A DFT study of pyrazine derivatives and their Fe complexes in corrosion inhibition process, J. Mol. Struct. 1086 (2015) 64−72.
[34] S. Erdogan, Z.S. Safi, S. Kaya, D. Özbakır Isin, L. Guo, C. Kaya, A computational study on corrosion inhibition performances of novel quinoline derivatives against the corrosion of iron , aban erdo, G. *J. Mol. Struct.* 1134 (2017) 751−761.
[35] A. Zarrouk, B. Hammouti, T. Lakhlifi, M. Traisnel, H. Vezin, F. Bentiss, New 1 H -Pyrrole-2 , 5-dione derivatives as efficient organic inhibitors of carbon steel corrosion in hydrochloric acid Medium: electrochemical , XPS and DFT studies, Corrosion Sci. 69 (8) (2015) 1545−1555.
[36] D. Seifzadeh, A. Bezaatpour, A.N. Shamkhali, H. Basharnavaz, Experimental and theoretical studies to examine the inhibition effect of a schiff base against magnesium corrosion, Trans. Indian Inst. Met. 69 (2016) 1545−1555.
[37] D. Seifzadeh, S. Hamzedoust-Hasankiadeh, A.N. Shamkhali, Electrochemical and DFT studies of 8-hydroxyquinoline as corrosion inhibitor for AZ61 magnesium alloy in acidic media, Protect. Met. Phys. Chem. Surface 49 (2) (2013) 229−239.
[38] D.A. Winkler, M. Breedon, A.E. Hughes, F.R. Burden, A.S. Barnard, T.G. Harvey, I. Cole, Towards chromate-free corrosion inhibitors: structure − property models for organic alternatives, Green Chem. 16 (2014) 3349−3357.
[39] N. Kovačević, I. Milošev, A. Kokalj, How relevant is the adsorption bonding of imidazoles and triazoles for their corrosion inhibition of Copper ? Corrosion Sci. 124 (2017) 25−34.
[40] A. Kokalj, Is the analysis of molecular electronic structure of corrosion inhibitors sufficient to predict the trend of their inhibition performance, Electrochim. Acta 56 (2) (2010) 745−755.
[41] A. Kokalj, D. Costa, in: K. Wandelt (Ed.), Encyclopedia of Interfacial Chemistry: Surface Science and Electrochemistry, Elsevier, 2018.
[42] R. Tan, Z. Lv, J. Tang, Y. Wang, J. Guo, L. Li, Theoretical study of the adsorption characteristics and the environmental influence of ornidazole on the surface of photocatalyst TiO 2, Sci. Rep. 9 (2019) 10891.
[43] M. Taheri, J.R. Kish, N. Birbilis, M. Danaie, E.A. Mcnally, J.R. Mcdermid, Towards a physical description for the origin of enhanced catalytic activity of corroding magnesium surfaces, Electrochim. Acta 116 (2014) 396−403.
[44] S. Fajardo, G.S. Frankel, Effect of impurities on the enhanced catalytic activity for hydrogen evolution in high purity magnesium, Electrochim. Acta 165 (2015) 255−267.
[45] G. Kresse, J. Hafner, Ab Initio molecular dynamics for liquid metals, Phys. Rev. B 47 (1993) 558.
[46] G. Kresse, J. Hafner, Ab Initio molecular-dynamics simulation of the liquid-metal-amorphous-semiconductor transition in germanium, Phys. Rev. B 49 (1994) 14251.
[47] G. Kresse, J. Furthmüller, Efficient iterative schemes for Ab Initio total-energy calculations using a plane-wave basis set, Phys. Rev. B 54 (1996) 11169−11186.
[48] G. Kresse, J. Fürthmüller, Efficiency of ab-initio total energy calculations for metals and semiconductors using a plane-wave basis set, Comput. Mater. Sci. 6 (1996) 15−50.
[49] W. Heckel, T. Würger, S. Müller, G. Feldbauer, Van der Waals interaction really matters: energetics of benzoic acid on TiO2 rutile surfaces, J. Phys. Chem. C 121 (2017) 17207−17214.
[50] J. Klimeš, D.R. Bowler, A. Michaelides, Chemical accuracy for the van Der Waals density functional, J. Phys. Condens. Matter 22 (2010), 022201.
[51] J. Klimeš, D.R. Bowler, A. Michaelides, Van der Waals density functionals applied to solids, Phys. Rev. B 83 (2011) 195131.
[52] G. Román-Pérez, J.M. Soler, Efficient implementation of a van Der Waals density functional: application to double-wall carbon nanotubes, Phys. Rev. Lett. 103 (2009), 096102.
[53] T. Thonhauser, V.R. Cooper, S. Li, A. Puzder, P. Hyldgaard, D.C. Langreth, Van der Waals density functional: self-consistent potential and the nature of the van Der Waals bond, Phys. Rev. B 76 (2007) 125112.
[54] M. Dion, H. Rydberg, E. Schröder, D.C. Langreth, B.I. Lundqvist, Van der Waals density functional for general geometries, Phys. Rev. Lett. 92 (2004) 246401.
[55] G. Graziano, J. Klimeš, F. Fernandez-Alonso, A. Michaelides, Improved description of soft layered materials with van Der Waals density functional theory, J. Phys. Condens. Matter 24 (2012) 424216.
[56] P.O. Bedolla, G. Feldbauer, M. Wolloch, C. Gruber, S.J. Eder, N. Dörr, P. Mohn, J. Redinger, A. Vernes, Density functional investigation of the adsorption of isooctane, ethanol, and acetic acid on a water-covered Fe(100) surface, J. Phys. Chem. C 118 (2014) 21428−21437.
[57] P.O. Bedolla, G. Feldbauer, M. Wolloch, S.J. Eder, N. Dörr, P. Mohn, J. Redinger, A. Vernes, Effects of van Der Waals interactions in the adsorption of isooctane and ethanol on Fe(100) surfaces, J. Phys. Chem. C 118 (2014) 17608−17615.
[58] M. Antlanger, W. Mayr-Schmölzer, J. Pavelec, F. Mittendorfer, J. Redinger, P. Varga, U. Diebold, M. Schmid, Pt 3 Zr(0001): a substrate for growing well-ordered ultrathin zirconia films byoxidation, Phys. Rev. B 86 (2012), 035451.
[59] J.I.J. Choi, W. Mayr-Schmölzer, F. Mittendorfer, J. Redinger, U. Diebold, M. Schmid, The growth of ultra-thin zirconia films on Pd 3 Zr(0001), J. Phys. Condens. Matter 26 (2014) 225003.
[60] J. Carrasco, W. Liu, A. Michaelides, A. Tkatchenko, Insight into the description of van Der Waals forces for benzene adsorption on transition metal (111) surfaces, J. Chem. Phys. 140 (2014), 084704.
[61] J. Matos, H. Yildirim, A. Kara, Insight into the effect of long range interactions for the adsorption of benzene on transition metal (110) surfaces, J. Phys. Chem. C 119 (2015) 1886−1897.
[62] T. Würger, W. Heckel, K. Sellschopp, S. Müller, A. Stierle, Y. Wang, H. Noei, G. Feldbauer, Adsorption of acetone on rutile TiO2: a DFT and FTIRS study, J. Phys. Chem. C 122 (34) (2018) 19481−19490.
[63] F. Mittendorfer, A. Garhofer, J. Redinger, J. Klimeš, J. Harl, G. Kresse, Graphene on Ni (111): strong interaction and weak adsorption, Phys. Rev. B 84 (2011) 201401.
[64] W. Liu, J. Carrasco, B. Santra, A. Michaelides, M. Scheffler, A. Tkatchenko, Benzene adsorbed on metals: concerted effect of covalency and van Der Waals bonding, Phys. Rev. B 86 (2012) 245405.
[65] M. Endlich, A. Michl, J. Hildisch, S. Müller, J. Kröger, Energy and spectroscopic line shape of the C-O stretch mode on Ir (111) in the presence of organic molecules, J. Phys. Chem. C 120 (2016) 11490−11497.
[66] H.J. Monkhorst, J.D. Pack, Special points for brillouin-zone integrations, Phys. Rev. B 13 (1976) 5188.
[67] P. Blöchl, O. Jepsen, O. Andersen, Improved tetrahedron method for brillouin-zone integrations, Phys. Rev. B 49 (1994) 16223−16233.
[68] A. Vittadini, A. Selloni, F.P. Rotzinger, M. Grätzel, Formic acid adsorption on dry and hydrated TiO2 anatase (101) surfaces by DFT calculations, J. Phys. Chem. B 104 (6) (2000) 1300−1306.
[69] J. Oviedo, M. San, J. Sanz, Oxygen vacancies on TiO 2 (110) from first principles calculations, J. Chem. Phys. 121 (2004) 7427−7433.
[70] G. Makov, M. Payne, Periodic boundary conditions in Ab Initio calculations, Phys. Rev. B 51 (1995) 4014.
[71] J. Neugebauer, M. Scheffler, Adsorbate-substrate and adsorbate-adsorbate interactions of Na and K adlayers on Al (111), Phys. Rev. B 46 (1992) 16067.
[72] M. Jönsson, D. Persson, C. Leygraf, Atmospheric corrosion of field-exposed magnesium alloy AZ91D, Corrosion Sci. 50 (2008) 1406−1413.
[73] R. Valdez, J. Manuel, Q. Melgoza, Nanosheets of Co- (Ni and Fe) layered double hydroxides for electrocatalytic water oxidation reaction, Int. J. Electrochem. Sci. 10 (2015) 909−918.
[74] S.V. Lamaka, J. Gonzalez, D. Mei, F. Feyerabend, R. Willumeit-römer, M.L. Zheludkevich, Local PH and its evolution near Mg alloy surfaces exposed to simulated body fluids, Adv. Mater. Interfaces 1800169 (5) (2018).
[75] A.E. Martell, R.M. Smith, Critical Stability Constants, Amino Acids, vol. 1, Springer, New York, 1974.
[76] A.E. Martell, R.M. Smith, Critical Stability Constants, Other Organic Ligands, vol. 3, Springer, New York, 1977.
[77] A.E. Martell, R.M. Smith, Critical Stability Constants: Second Supplement, vol. 6, Springer Science & Business Media, 1989.
[78] J.A. Dean, Lange's Handbook of Chemistry, McGraw-Hill, Inc., New York; London, 1999. New york; London: McGraw-Hill, Inc.
[79] E.P.M. van Westing, G.M. Ferrari, J.H.W. de Wit, The determination of coating performance with impedance measurements-III. In situ determination of loss of adhesion, Corrosion Sci. 36 (6) (1994) 979−994.
[80] E.P.M. van Westing, G.M. Ferrari, J.H.W. de Wit, The determination of coating performance with impedance measurements-I. Coating polymer properties, Corrosion Sci. 34 (9) (1993) 1511−1530.
[81] A. Maltseva, Evolution de Surface Lors de La Corrosion de Magnésium: Nouvelles Approches Analytiques Pour Comprendre Les Mécanismes de Corrosion et de Protection, ChimieParis/ParisTech, 2018.
[82] A. Maltseva, S.V. Lamaka, K.A. Yasakau, D. Mei, D. Kurchavov, M.L. Zheludkevich, G. Lefèvre, P. Volovitch, In situ surface film evolution during Mg aqueous corrosion in presence of selected carboxylates, Corrosion Sci. (2020) 108484.
[83] Tackett, J. E. FT-IR characterization of metal acetates in aqueous solution, Appl. Spectrosc. 43 (3) (1989) 483−489.
[84] J. Friedrich, Metal-Polymer Systems: Interface Design and Chemical Bonding, Wiley-VCH Verlag GmbH & Co., 2018.